Ellipsometry of Colloidal Solutions

Yann Battie, Michel Stchakovsky, Aotmane En Naciri, Suzanna Akil, Nouari Chaoui, Laurent Broch

Ellipsometry of Colloidal Solutions: New Experimental Setup and Application to Metallic Colloids

Yann Battie*, Michel Stchakovsky, Aotmane En Naciri, Suzanna Akil, Nouari Chaoui, and Laurent Broch,

Abstract

An ellipsometric cell is developed to simultaneously determine the shape distribution, the volume fraction, and the complex refractive index of gold and silver colloids. Simulation reveals that this cell drastically improves the detection limit of ellipsometry. Indeed, Ag and Au nanoparticles (NPs) are detected at the ppmv level. We demonstrate that the NPs shape distribution can be estimated from ellipsometric measurements by analyzing them with a shape distributed effective medium theory (SDEMT). The obtained distributions from ellipsometry are in agreement with those deduced from transmission electron microcopy (TEM). Contrary to TEM, ellipsometry probes a large number of NPs estimated at about 1011 NPs. Finally, we show that the complex refractive index of colloids as determined from ellipsometry is sensitive to the optical properties of the solvent and the plasmonic properties of NPs.

Introduction

Metallic colloids (NPs), such as Ag or Au NPs, have promising potential as building blocks of chemical sensors (1-4) or white light processing devices. (5, 6) These colloids exhibit unique optical properties such as plasmon resonance, which comes from the collective oscillation of their free electrons. (7-9) The characteristics of the plasmon resonance mainly depend on the NPs shape, the interparticle distance, and the refractive index of the matrix. (7-10) Thus, the control of NPs shape distribution is a bottleneck in the development of devices based on metallic NPs. The NPs shape distribution is often determined from transmission electron microscopy. However, since transmission electron microscopy (TEM) is a local characterization tool, the distributions are obtained on a small number of NPs. Grazing incidence small-angle X-ray scattering (GISAXS) was also previously used to characterize the morphology of supported NPs. (11-13) The shape distribution can be estimated by comparing the measured GISAXS pattern with the simulated one. However, this technique requires some facilities such as a synchrotron beamline which prevents its use for routine postsynthesis characterization. This limitation makes crucial the development of a nonlocal alternative characterization tool to determine the shape distribution of colloidal NPs.

Optical absorption spectroscopy has been recently exploited to gain quantitative insights on colloids. Indeed, as shown by Eustis and El-Sayed, (14) the aspect ratio distribution of Au nanorods can be evaluated by fitting their longitudinal plasmon band by the Gans theory. This approach has been validated by Slyusarenko et al. (15) by comparing the NP volume fraction obtained from absorption spectroscopy to the estimated one by small angle X-ray scattering measurement. However, the analysis of the absorption spectra with the Gans theory is limited to prolate NPs. A larger panel of NP shapes such as spherical, oblate, prolate, or nondegenerate ellipsoidal NPs was recently considered by using a shape distributed effective medium theory (SDEMT). (16-19) However, since absorption spectroscopy is only sensitive to the extinction coefficient, the previous knowledge of the refractive index of the NP environment is required to exploit the absorption spectra of colloids with the SDEMT

theory. The determination of this refractive index is a nontrivial issue since it depends on the solvent, surfactant or counterions used during the NPs synthesis.

Ellipsometry is an indirect characterization tool based on the change of the polarization state of light after reflection on the sample. Unlike absorption spectroscopy, ellipsometry is sensitive to both real and imaginary parts of the refractive index of the materials. For this reason, spectroscopic ellipsometry has been extensively used to characterize Au or Ag NPs embedded in thin films such as polymer, (20-22) TiO2, (23) or SiO2 (24, 25) or deposited on a surface. (26-28) Kubo et al. (29) have also reported ellipsometric measurements on alkanethiol-capped Au NPs dispersed in a n-dodecane solution. The ellipsometric spectra were recorded on a single liquid/air interface. Despite the incommensurate volume fraction of NPs used by the authors (2500–7500 ppmv), these measurements suffered from a low signal-to-noise ratio. Note that the volume fraction of standard colloidal solutions is 3–4 orders of magnitude smaller than that reported in the work of Kubo et al., (29) which is close to the critical aggregation concentration. This suggests that ellipsometry is not adapted yet for the characterization of colloidal solutions and its detection limit must be improved to detect small NP volume fraction.

In this paper, we have developed a specific cell for ellipsometric measurements on Au and Ag colloidal solutions. Contrary to classical ellipsometric cells used to characterize solid–liquid or liquid–liquid interfaces, (30-35) our cell design pushes the detection limit of ellipsometry to NPs toward the ppmv range required to characterize colloidal solutions. The complex effective refractive index of the colloids as well as the volume fraction and the shape distribution of NPs have been deduced from an analysis of the ellipsometric measurements using an effective medium theory which takes into account the NPs shape distribution. In the following, we demonstrate that these distributions, obtained from a sampling of 10^{11} NPs, are close to those deduced from TEM and that ellipsometry coupled to the liquid cell enables the determination of the shape distribution, the concentration and the optical properties of Au or Ag colloids.

Materials and Methods

In this paper, three colloidal solutions of gold NPs (Au1, Au2, Au3) and one colloidal solution of silver NPs (Ag1) are considered.

For the Au1 synthesis, 65 mg of sodium citrate in 100 mL of water was added to 1 mL of aqueous solution containing 9.5 mg HAuCl4. The solution was boiled during 15 min.

Gold nanorods were fabricated by seed-mediated growth method. Thus, seed and growth solutions were made according to the following process. A volume of 5 mL of 5 × 10–4 M HAuCl4 was mixed with 5 mL of CTAB solution of 0.2 M. Under stirring, 0.6 mL of ice-cold 0.01 M NaBH4 was added to this solution, which allowed the formation of seed solution. This solution was then vigorously stirred during 2 min and stored during at least 2 h at 25 °C. To allow the formation of gold nanorods (Au2 and Au3 solutions), 5 mL of CTAB (0.2 M) was added to 210 µL (Au2) and 170 µL (Au3) of 4 × 10–3 M AgNO3 solution at 28 °C. To this solution, 5.0 mL of 10–3 M HAuCl4 was added. Successively, 70 µL of 0.08 M ascorbic acid was added under gentle stirring. Then, the pH was adjusted by adding NaOH (0.2 M) to change the growth solution from dark yellow to colorless. Finally, 20 µL of the seed solution was added to the growth solution. The solution gradually turned to violet within 10–20 min, indicating the rod formation.

Arabinogalactan-protein (AGP) was used as reducing and capping agent to synthesize the Ag1 colloïds in a green manner. AGP is a high molecular weight polyelectrolyte (106 Da) that contains ∼1300

negative charges in aqueous medium, which is suitable for spontaneous fabrication of metallic nanoparticles. Stock dispersion of AGP was prepared by gradually adding the freeze-dried biopolymer to ultrapure deionized water under gentle stirring at 20 ± 1 °C for at least 2 h at 3 wt % biopolymer concentration. Subsequently, AGP dispersion was stored at 4 ± 1 °C during 24 h to allow good hydration of AGP polymer chain. The final pH was adjusted to 4.2 using 0.1 M HCl in order to obtain a maximum charge density on AGP tails. Under stirring and cooling at 0 ± 1 °C, AgNO3 powder at 0.3 wt % was added to AGP dispersion. The colorless solution immediately turned into dark yellow one due to the formation of silver nanoparticles (Ag NPs). The size and density of Ag NPs obtained can be adjusted by tuning the AgNO3/AGP ratio and the pH of the AGP solution.

Characterization

TEM was performed with a Technai CM200 microscope operating at 200 kV. TEM grids were prepared by evaporating a drop of colloidal solution on a copper grid.

Ellipsometric measurements were recorded at room temperature with a phase modulation ellipsometer (UVISEL, HORIBA Jobin Yvon) in the 1.4–3 eV and 1.5–4.5 eV spectral ranges for Au and Ag colloids, respectively. This device uses fixed polarizing elements. This configuration is required for accurate measurements on liquids to avoid any vibrations which can disturb the liquid surface. Two ellipsometric parameters Is and Ic which depend on the ellipsometric angles Ψ and Δare measured.

$$I_s = \sin 2\Psi \sin \Delta \quad (1)$$

$$I_c = \sin 2\Psi \cos \Delta \quad (2)$$

A liquid cell was used for ellipsometric measurements on liquids. The schematic representation of the cell is depicted in Figure 1. The liquid under study is sandwiched between the base of an isosceles silica prism with an angle of 55° and a silicon wafer. This ensures the absence of surface waves at both interfaces of the liquid. The thickness of the liquid is mechanically fixed by spacers which thicknesses can be varied within the range 50–400 µm. The spacers are electropolished Ni blades with three sets of thicknesses between 50 and 200 µm, certified within 1%. A channel in the PVC cell is made to introduce the liquid.

A liquid cell was used for ellipsometric measurements on liquids. The schematic representation of the cell is depicted in Figure 1. The liquid under study is sandwiched between the base of an isosceles silica prism with an angle of 55° and a silicon wafer. This ensures the absence of surface waves at both interfaces of the liquid. The thickness of the liquid is mechanically fixed by spacers which thicknesses can be varied within the range 50–400 µm. The spacers are electropolished Ni blades with three sets of thicknesses between 50 and 200 µm, certified within 1%. A channel in the PVC cell is made to introduce the liquid.

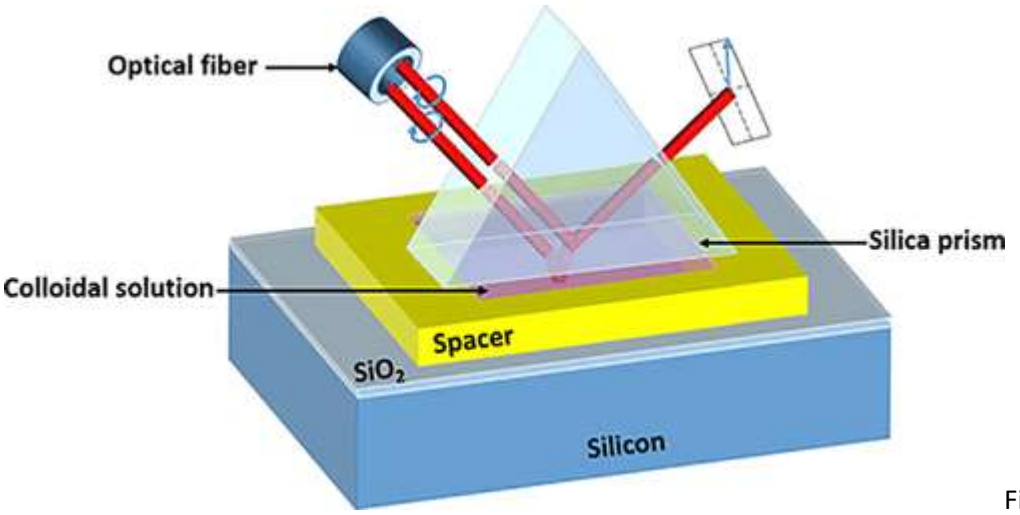

Figure 1

Figure 1. Schematic representation of the liquid cell.

Theory

Effective Medium Theory

Colloidal solutions are composed of ellipsoidal nanoparticles distributed in shape and randomly oriented in the solvent. Their optical properties are described by an effective dielectric function defined as the ratio between the spatial averages of displacement ⟨D⟩ and electric ⟨E⟩ fields:

$$\varepsilon_{\text{eff}} = \langle \mathbf{D} \rangle \langle \mathbf{E} \rangle^{-1} \quad (3)$$

The spatial averages of displacement ⟨D⟩ and electric ⟨E⟩ fields are the sum of two contributions: (16)

$$\langle \mathbf{D} \rangle = (1 - f)\varepsilon_{\text{m}} \langle \mathbf{E}_{\mathbf{m}} \rangle + f\varepsilon_{\text{np}} \langle \mathbf{E}_{\mathbf{np}} \rangle \quad (4)$$

$$\langle \mathbf{E} \rangle = (1 - f)\langle \mathbf{E}_{\mathbf{m}} \rangle + f\langle \mathbf{E}_{\mathbf{np}} \rangle \quad (5)$$

εnp and εm are the complex dielectric function of NPs and the matrix, respectively. f is the volume fraction of NPs. ⟨Em⟩ and ⟨Enp⟩ are the spatial average electric field inside the matrix and NPs, respectively. In the following, the dielectric function of metallic NPs is given by Palik (36) while the dielectric function of the matrix is described by a Lorentzian oscillator, assuming a transparent medium:

$$\varepsilon_{\text{m}} = 1 + \frac{(\varepsilon_{\text{s}} - 1)\omega_{\text{t}}^{\,2}}{\omega_{\text{t}}^{\,2} - \omega^{2}} \quad (6)$$

ωt is the transition energy of the oscillator, ω is the photon energy, and εs is the static dielectric function. In the quasi-static limit, i.e., for NP size smaller than the wavelength, a linear relationship is found between the electric field inside NPs and the electric field inside the matrix. By considering small volume fraction of NPs, the electric field inside the matrix is homogeneous and the spatial average electric field inside the NPs is given by

$$\langle \mathbf{E}_{\mathbf{np}} \rangle = \langle \beta \rangle \langle \mathbf{E}_{\mathbf{m}} \rangle \quad (7)$$

The slope ⟨β⟩ is calculated by (16)

$$\langle\beta\rangle = \frac{\varepsilon_m}{3} \iint P(L_1, L_2) \sum_{i=1}^{3} \frac{1}{\varepsilon_m + L_i(\varepsilon_{np} - \varepsilon_m)} dL_1\, dL_2 \quad (8)$$

L1, L2, L3 are the depolarization parameters of ellipsoidal NPs along their three principal axes and P(L1, L2) is their distribution. The depolarization parameters, which vary in the 0–1 range, are related to the length (a1, a2, a3) of principal axes of each ellipsoidal NP: (19)

$$\langle\beta\rangle = \frac{\varepsilon_m}{3} \iint P(L_1, L_2) \sum_{i=1}^{3} \frac{1}{\varepsilon_m + L_i(\varepsilon_{np} - \varepsilon_m)} dL_1\, dL_2 \quad (9)$$

where Ri =ai/a1 (i = 1, 2, 3) the aspect ratios of NPs. To obtain a bijective space, the lengths of principal axes are sorted by considering the Bohren convention: (37)a3 ≤ a2 ≤ a1. In addition, the depolarization parameters must respect the following sum rule: (37)

$$1 = L_1 + L_2 + L_3 \quad (10)$$

The effective dielectric function of a medium composed of ellipsoidal NPs embedded in a dielectric matrix can be calculated by combining eqs 3–5 and 7: (16)

$$\varepsilon_{eff} = \frac{(1-f)\varepsilon_m + f\varepsilon_{np}\langle\beta\rangle}{(1-f) + f\langle\beta\rangle} \quad (11)$$

This equation is the fundamental equation of the shape distributed effective medium theory (SDEMT). Note that this theory, which is based on the quasistatic approximation, is only valid for NPs size smaller than the wavelength. In addition, the volume fraction of NPs must be small enough to neglect the interaction between NPs.

Models

Two distinct physical models were considered to analyze the ellipsometric data (Figure 2). The first model (M1) is introduced to simulate ellipsometric spectra recorded on a single liquid/air interface. The liquid is considered as a semi-infinite substrate. The refractive index of the ambient and the angle of incidence are set at 1 and 55°, respectively. The second model (M2) is used to interpret ellipsometric spectra recorded with the liquid cell. This model consists in a silicon substrate covered by a native silicon oxide layer and a liquid layer. The thickness of the silicon oxide layer is about 3 nm, while the thickness of the liquid layer is set by the thickness of spacers. Silica is used as ambient. The angle of incidence of light, defined by the angle of the prism is 55°. The complex index of refraction of liquid is calculated by the SDEMT theory (11). The indexes of refraction of silica and silicon substrate come from the Palik data. (36)

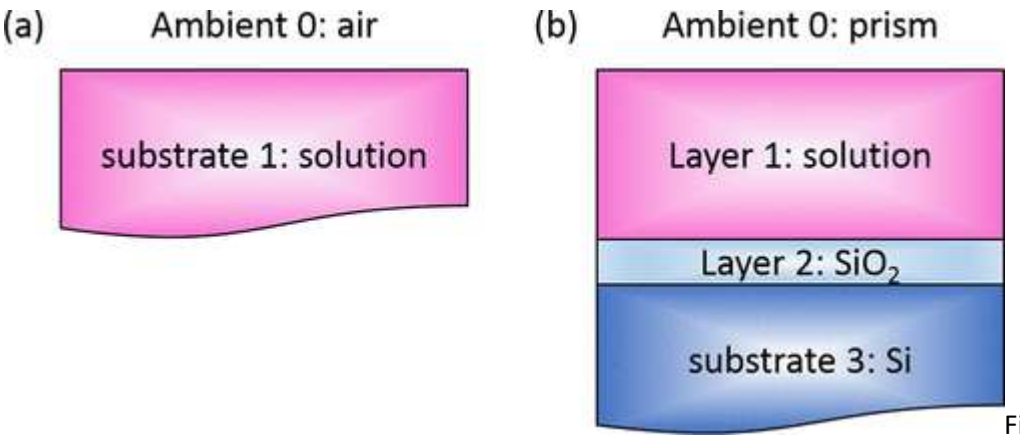

Figure 2

Figure 2. Schematic representation of the (a) M1 and (b) M2 models used to exploit ellipsometric measurements recorded in configurations C1 and C2, respectively.

To make an accurate calculation of ellipsometric spectra, the film thickness must be compared to the coherence length L of the ellipsometer. The coherence length of light L is defined by

$$L = \frac{\lambda^2}{2n_1 \cos\theta_1 \, \Delta\lambda} \quad (12)$$

where Δλ = 4 nm is the wavelength resolution of the ellipsometer, n1 is the refractive index of liquids at the wavelength λ, and θ1 is the angle of the refraction in the liquid. By assimilating the liquid as water, the coherence length at 400 nm is 34 µm. This value is smaller than the thickness of spacers. In other words, the thickness of liquid layer is thick enough to satisfy the incoherent reflection condition. Thus, the modeling consists of the incoherent summation of multiple reflected beams, adding their contributions in terms of intensities. As illustrated in Figure 1, two beams are collected by the optical fiber of the ellipsometer: the beam reflected at the prism/liquid interface and the beam which comes from the first reflection at the liquid/silicon substrate interface.

The ellipsometric parameters Is and Ic, which correspond to the m34 and m33 elements of the Mueller matrix of the Si/SiO2/liquid/prism system, are calculated as follows: (38-40)

$$I_s = \frac{2Im(r_p r_s^*)}{|r_p|^2 + |r_s|^2} \quad (13)$$

$$I_c = \frac{2Re(r_p r_s^*)}{|r_p|^2 + |r_s|^2} \quad (14)$$

where

$$|r_p|^2 = |r_{p01}|^2 + |t_{p01}|^2 |t_{p10}|^2 |r_{p123}|^2 \, e^{-4Im(\beta)} \quad (15)$$

$$|r_s|^2 = |r_{s01}|^2 + |t_{s01}|^2 |t_{s10}|^2 |r_{s123}|^2 \, e^{-4Im(\beta)} \quad (16)$$

$$r_p r_s^* = r_{p01} r_{s01}^* + t_{p01} t_{p10} r_{p123} t_{s01}^* t_{s10}^* r_{s123}^* \, e^{-4Im(\beta)} \quad (17)$$

$$\beta = 2\pi\frac{h}{\lambda}n_1 \cos\theta_1 \quad (18)$$

h is the thickness of the liquid layer. θ1 is the angle of refraction of light in the liquid. ri01, ti01, and ti10 (i = p, s) stand for the reflection and the transmission Fresnel coefficients of p and s polarized light at the prism/liquid interface. ri123 is the reflection Fresnel coefficient of i = p, s polarized light of the Si/SiO2 substrate, considering the liquid as the ambient. The term e–4Im(β) denotes the absorption of light in the liquid layer.

Results and Discussion

To evaluate the detection limit of ellipsometry, the spectra of spherical Au and Ag NPs dispersed in water are simulated in the 1.55 eV-4.14 eV spectral range by considering two configurations. The first one (C1) corresponds to ellipsometric spectra recorded on a single liquid/air interface without ellipsometric cell. These spectra are simulated with model M1. The second configuration (C2) corresponds to ellipsometric spectra recorded with the liquid cell. In this configuration, simulations are made with model M2 by considering three spacer thicknesses: 50, 100, and 400 μm. The effective dielectric function of the colloidal solution is calculated by using SDEMT (11). To simulate a distribution of monodispersed spherical NPs, we consider that the distribution of depolarization factor is given by

$$P(L_1, L_2) = \delta(1/3, 1/3) \quad (19)$$

δ is the Dirac distribution. The NPs volume fraction f varies in the 1–500 ppmv range. The sensitivity of ellipsometric spectra to NPs is quantified by calculating the mean variations of ellipsometric spectra, in the 1.5–4.15 eV spectral range, induced by the presence of NPs:

$$\delta_0(f) = \sqrt{\frac{1}{2N}\sum_{i=0}^{N}(\Psi(f,\lambda_i) - \Psi(0,\lambda_i))^2 + (\Delta(f,\lambda_i) - \Delta(0,\lambda_i))^2} \quad (20)$$

Ψ(f,λi) and Δ(f,λi) are the ellipsometric angles simulated at the wavelength λi for a NP volume fraction f. In configuration C1, the ellipsometric angles are simulated by considering the solution as a semi-infinite substrate (38) while in configuration C2 the ellipsometric angles are determined from eqs 15–18. The function δ0(f) is represented in Figure 3a and b.

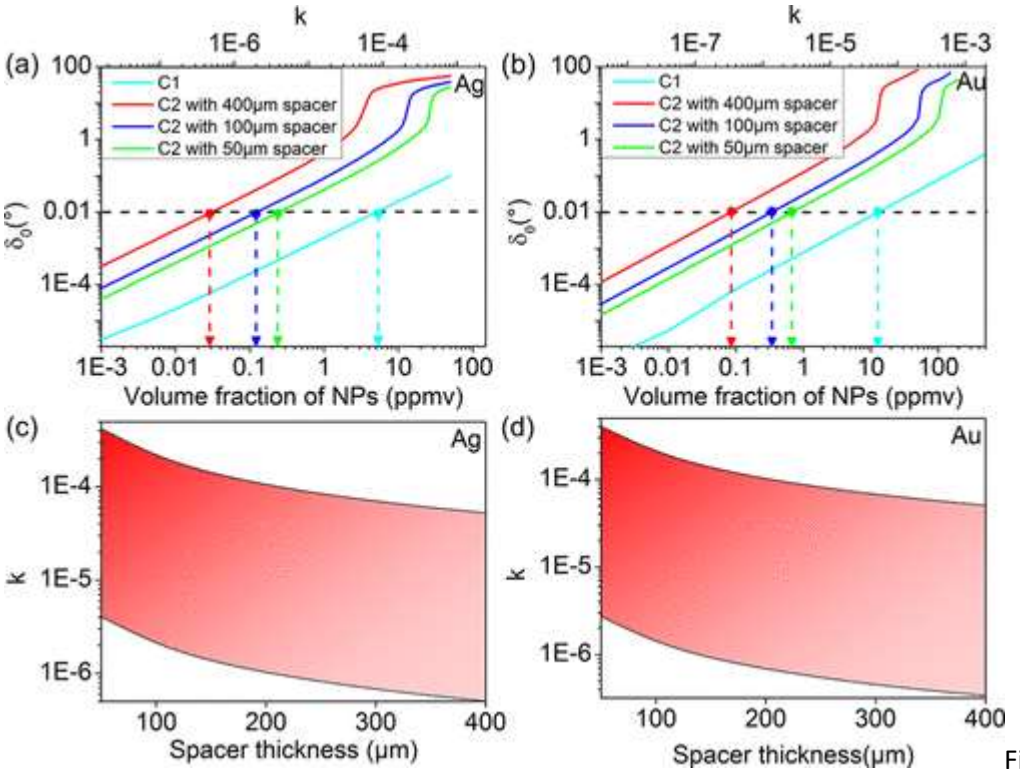

Figure 3

Figure 3. (a,b) Mean variations of ellipsometric spectra induced by the presence of monodispersed spherical (a) Ag and (b) Au NPs as a function of their volume fraction and extinction coefficient at the plasmon resonance. (c,d) Evolution of the limit of sensitivity in term of extinction coefficient of (c) Ag and (d) Au colloids with the spacer thickness. The domain of sensitivity of our ellipsometric setup is represented in red.

For the C1 configuration, a linear relationship is found between δ0 and the volume fraction. A linear variation, with the same slope, is also observed for the C2 configuration at low volume fraction, suggesting that both configurations have similar sensitivity. However, an abrupt increase is observed in configuration C2 for δ0 higher than 4. This behavior, which occurs for high NP volume fractions, is explained by the almost complete absorption of the beam inside the liquid layer in the vicinity of the plasmon resonance energy. Indeed, the Stokes parameter S0 at the plasmon resonance, which represents the total reflected light, becomes smaller than 7% for δ0 higher than 4. This defines the highest concentration limit that can be measured by the ellipsometric cell. The accuracy of the ellipsometer on Ψ and Δ is 0.01°. The detection limit of ellipsometric measurements is determined when the condition δ0(f) = 0.01° is fulfilled. The detection limit of ellipsometric measurements performed on a single air/liquid interface (condition C1) is estimated at 10 and 5 ppmv for Au and Ag NPs, respectively. These values are probably underestimated because the air/liquid interface is highly sensitive to perturbations. Thus, measurements performed on a single air/liquid interface suffer from lack of sensitivity. This result, which is in agreement with the low signal-to-noise ratio observed by Kubo et al., (29) is also supported by measurements performed on colloids in configuration C1 (see the Supporting Information (Figure S1)). To push the detection limit toward the subppm resolution, the use of an ellipsometric cell is required. By using a 400 µm spacer, the detection limit decreases by 2 orders of magnitude. Indeed, it reaches 0.09 and 0.03 ppmv for Au and Ag NPs, respectively. These detection limits are calculated for monodispersed spherical NPs in water. However, the ellipsometric

spectra and so the detection limit in term of NPs concentration, depend on the NP shape distribution. Therefore, the most relevant parameter is the smallest extinction coefficient that we can measure. (41) The range of the extinction coefficient of colloidal solutions that can be measured with the ellipsometric cell is reported in Figure 3c and d. For a 400 μm spacer, the detection limit, in terms of extinction coefficient of the colloidal solution, is estimated to 4 × 10–7. In addition, the detection limit increases as the spacer thickness decreases. In other words, the absorption of the light beam during its propagation in the liquid enables a very significant improvement of the detection limit of NPs compared to that obtained from measurements on a single liquid/air interface.

The TEM images of Au1, Ag1, Au2, and Au3 are depicted in the Supporting Information (Figure S2). The measured length and the distributions of the minor (d) and major (D) axes of NPs are reported in Figure 4. Au1 and Ag1 are composed of spherical NPs. Their mean diameters are estimated at 8.6 ± 3.5 and 5.8 ± 2.3 nm, respectively. Au2 and Au3 are composed of two populations of Au NPs. Indeed, both solutions are composed of a mixture of gold nanorods and spherical nanoparticules. The length of the minor axis of Au2 and Au3 nanorods is estimated at 5–8 nm, while the length of their major axis is in the 5–40 nm range. The diameter of spherical NPs is in the 13–28 nm range.

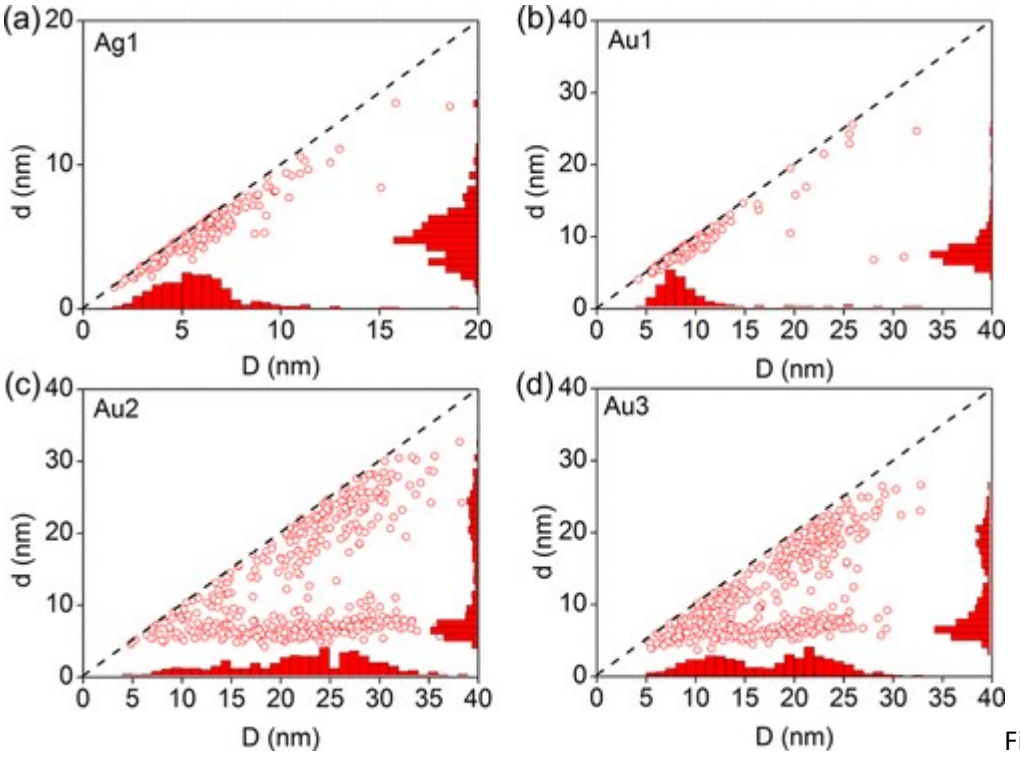

Figure 4

Figure 4. Distributions of the smallest (d) and largest (D) apparent diameter of (a) Ag1, (b) Au1, (c) Au2, and (d) Au3 NPs measured by TEM.

The aspect ratio distributions of Ag1, Au1, Au2, and Au3, measured on more than 250 NPs, are reported in the Figure 5. Note that the aspect ratio is defined as the ratio between the smallest and the largest apparent diameter of NPs. In accordance with TEM measurements (Figure 4), the aspect ratios of Au1 and Ag1 NPs are close to 1. Au2 and Au3 are composed of a mixture of nanorods and slightly elongated NPs. The mean values of aspect ratio of Au2 and Au3 nanorods are 0.25 ± 0.03 and

0.32 ± 0.05, respectively. The mean values of the aspect ratio of slightly elongated Au2 and Au3 NPs are 0.95 ± 0.15 and 0.82 ± 0.15, respectively.

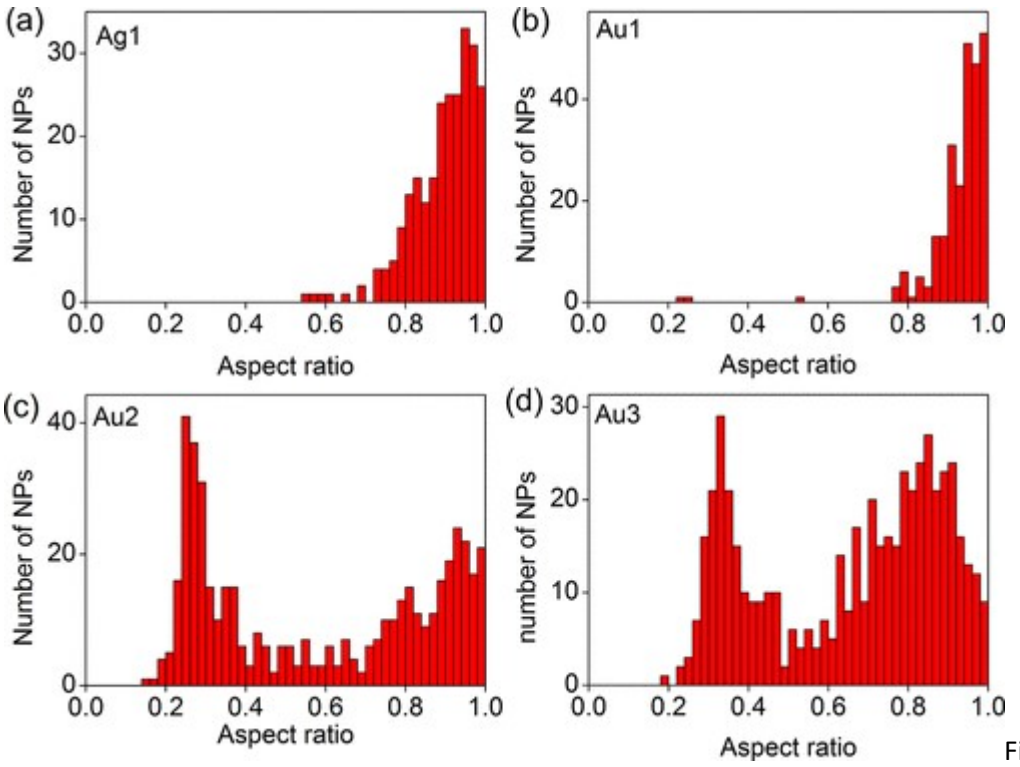

Figure 5

Figure 5. Apparent aspect ratio distribution measured by TEM of (a) Ag1, (b) Au1, (c) Au2, and (d) Au3.

The ellipsometric measurements performed with the liquid cell on Ag1, Au1, Au2, and Au3 are shown in Figure 6. The thickness of the spacers is 300 µm for Ag1 and 400 µm for Au1, Au2, and Au3. Thus, the volume of solutions required for ellipsometric measurements is estimated to 25 µL for Ag1 and 34 µL for Au1, Au2, and Au3. The ellipsometric spectra of Ag1 and Au1 have a single band centered at 2.9 and 2.3 eV, respectively. On the other hand, the ellipsometric spectra of Au2 and Au3 have two bands located at 2.3 eV and in the 1.55–1.8 eV range. These bands are the optical fingerprints of Ag and Au NPs in water. In other words, by using the liquid cell (configuration C2), the detection limit is small enough and the signal-to-noise ratio is sufficiently high to detect NPs in colloidal solution.

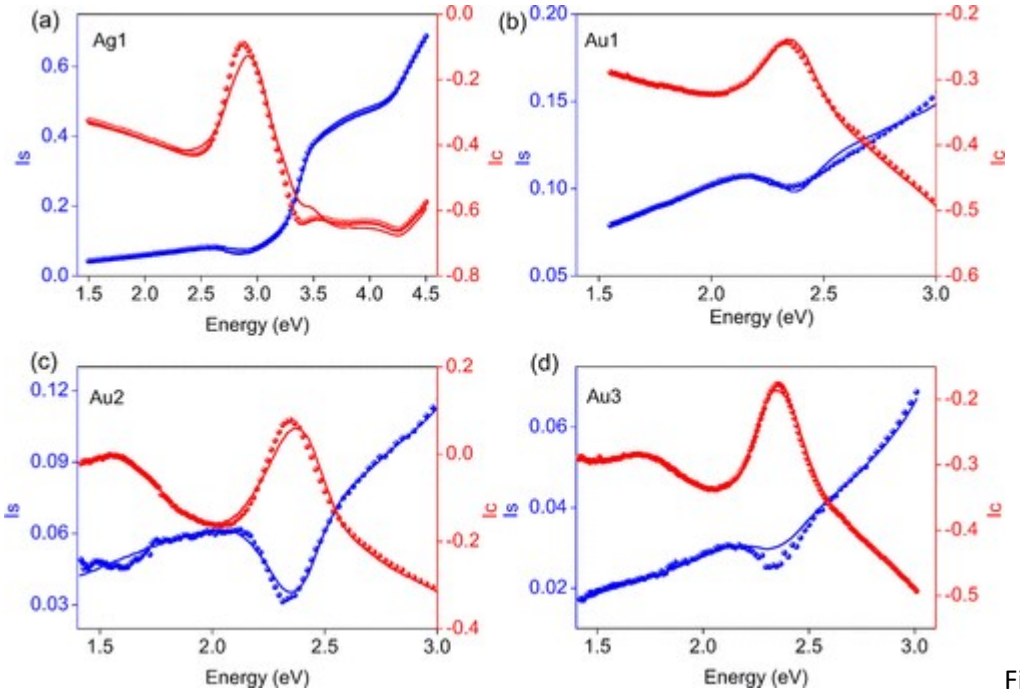

Figure 6

Figure 6. Comparison between ellipsometric measurements (dot) recorded on (a) Ag1, (b) Au1, (c) Au2, and (d) Au3 with the ellipsometric cell and the calculated data (solid line).

The limitations of ellipsometric characterization should be addressed to evaluate the correctness of our fitting procedure. The main drawback of ellipsometry is that the interpretation of the spectra is not very intuitive and the fitting of the spectra with an erroneous optical model can lead to erroneous interpretation. Therefore, the model used to exploit ellipsometric data must be physical and must takes into account the main characteristics, which influence the optical properties of materials. In the following, the SDEMT theory is used to extract the NPs shape distribution from ellipsometric spectra. However, we must keep in mind that this model has several limitations. Indeed, it does not take into account the presence of surfactant shell, surface roughness or NP size effects. In addition, this model is only valid for small NPs particle volume fraction to neglect the interaction between NPs and to avoid their aggregation. Thus, the error on the nanoparticle shape distribution induced by the limit of this model must be evaluated. In this paper, the colloidal solutions are sufficiently diluted to neglect the interaction between NPs. In addition, as shown by Trügler et al., (42) the surface roughness of NPs has a negligible effect on the far field optical response of NPs. To evaluate the influence of the NP size, we simulated from the Mie theory (37) the spectra of spherical Au and Ag NPs in water by taking into account confinement effect. (7) The NP size vary in the 2–40 nm range while the NP volume fraction is set at 10 ppmv. These spectra are then fitted with the SDEMT theory, and the errors on the mean value of aspect ratio and the volume fraction induced by size effect are then calculated. These errors are estimated at 4% and 5%, respectively. The same procedure is used to evaluate the error induced by the presence of a surfactant shell. The spectra of spherical gold and silver NPs with a CTAB shell are simulated from the generalized Mie theory (37) and then fitted with the SDEMT theory. Water is used as the matrix. The thickness and the refractive index of the CTAB layer are 1.5 nm and 1.435, respectively. (43, 44) The metallic core diameter vary in the 2–40 nm range while the volume fraction of NPs is set to 10 ppmv. We conclude from these simulations that the error on the aspect ratio and volume fraction induced by the presence of CTAB shell is negligible compared to the error induced by

size effect. This behavior is explained by the small contrast between the refractive index of water and CTAB as well as the small thickness of the CTAB shell. In addition, a large number of dielectric constant data set of gold and silver are given in the literature. (36, 45, 46) The choice of dielectric constant data set is crucial to obtain relevant distribution. Indeed, as reported by Jiang et al., (46) the dielectric function of Ag given by Johnson and Christy gives erroneous plasmon band amplitude and width. Indeed, the distribution obtained from ellipsometric or transmission measurements dependents on the dielectric function data set. The absence of consensus in dielectric function data set could limit the application of our characterization procedure and must be addressed prior the modeling of ellipsometric data. By comparing some measured absorption spectra of spherical Au and Ag colloids to the simulated ones with the SDEMT model, we have concluded in our previous work that the Palik database (36) can be considered as a good trade-off. (17) Moreover, the choice between unimodal and bimodal NP distributions is also a crucial issue for the ellipsometric data analysis. Indeed, the quality of the fit depends on the chosen distribution. TEM can be used to select the distribution. In this work, the choice of the distribution is directly deduced from ellipsometric measurements. Indeed, a single plasmon band is observed on the Au1 and Ag1 spectra, so a unimodal distribution is used to analyze them. On the contrary, two plasmon bands are observed on the Au2 and Au3 spectra. The high amplitude of the band located at 2.3 eV suggests that these solutions are composed of two types of NPs: spherical nanoparticles and nonspherical NPs.

The ellipsometric spectra measured with the liquid cell are analyzed by using model M2. We assume that the distribution of depolarization parameters P(L1,L2) of the NPs is described as a sum of two Gaussian distributions: (19)

$$P(L_1, L_2) = C(A\, e^{-0.5((L_1-\overline{L}_{1,1})^2/\sigma_{1,1}^2+(L_2-\overline{L}_{2,1})^2/\sigma_{2,1}^2+(L_3-\overline{L}_{3,1})^2/\sigma_{3,1}^2)} + (1-A)e^{-0.5((L_1-\overline{L}_{1,2})^2/\sigma_{1,2}^2+(L_2-\overline{L}_{2,2})^2/\sigma_{2,2}^2+(L_3-\overline{L}_{3,2})^2/\sigma_{3,2}^2)}) \quad (21)$$

C is a constant used to normalize the distribution. $\overline{L}i,k$ and σi,k (i = 1, 2, 3 and k = 1, 2) are the mean value and the standard deviation of Li of the kth Gaussian term, respectively. $\overline{L}1,k$, $\overline{L}2,k$, and $\overline{L}3,k$ are linked with each other according to eq 10. A is a parameter which varies in the 0–1 range. According to TEM images (Figure 4) and ellipsometric sepectra (Figure 6), A is equal to 1 in the case of samples Ag1 and Au1. In both cases, the fitted parameters are the mean values and standard deviations of P(L1, L2), the volume fraction f, ωt, and εs. On the contrary, the A parameter is also fitted for Au2 and Au3. In other words, 8 parameters are fitted for Au1 and Ag1 while 14 parameters are fitted for Au2 and Au3. All free parameters are simultaneously determined by using the Levenberg–Maquardt algorithm. (47) Levenberg–Marquardt algorithm is extremely sensitive to local minimum of the error function. In other words, the determination of initial guess is a crucial issue to avoid failing in local minimum. As we have reported previously, (16) the plasmon band position is mainly sensitive to the mean value of the depolarization factor. The plasmon band energy can be directly evaluated from the Ic ellipsometric spectra. Then, the initial guess of the mean values of depolarization factor is estimated from the plasmon band energy by using the Frohlich condition. (7) Since the solutions are highly diluted, the initial guess for the volume fraction of NPs is set to 0. The parameters ωt and εs are initialized to the 10.3 eV and 1.74, respectively. These values are obtained by fitting the dielectric function of water given by Palik. (36)

As shown in Figure 6, a good agreement is found between the measured and the calculated ellipsometric spectra. Indeed, the root-mean-square errors between the measured and calculated data are smaller than 0.02. In addition, all coefficients of the correlation matrix are smaller than 0.65, suggesting that all free parameters are independent. Indeed, as shown previously, each characteristic of the spectra is influenced by a specific free parameter. (16) As an example, the energy and width of

the plasmon band are directly related to the mean value and standard deviation of its corresponding depolarization parameter, respectively, while the UV spectral range is mainly influenced by the volume fraction of NPs. (16) The NP concentrations of Ag1, Au1, Au2, and Au3 are estimated to be 9.1 ± 0.5, 7.3 ± 0.4, 20.0 ± 1, and 10.0 ± 0.5 ppmv, respectively, confirming that NPs are sufficiently diluted to neglect their mutual interaction.

The distributions of the depolarization parameters obtained by ellipsometry are shown in Figure 7. In agreement with TEM measurements (Figure 4), the distribution of Au1 and Ag1 are close to the locus of spherical NPs (L1 = L2 = L3 = 1/3). In other words, this confirmed that Au1 and Ag1 are mainly composed of spherical NPs. The distributions of depolarization parameters of Au2 and Au3 are the combination of two Gaussian distributions centered on the locus of prolate NPs (L2 = L3 = 0.5(1 – L1)). Indeed, as shown in TEM images (Figure 4), these solutions contain a mixture of nanorods and slightly elongated NPs presenting the same symmetry as prolate NPs.

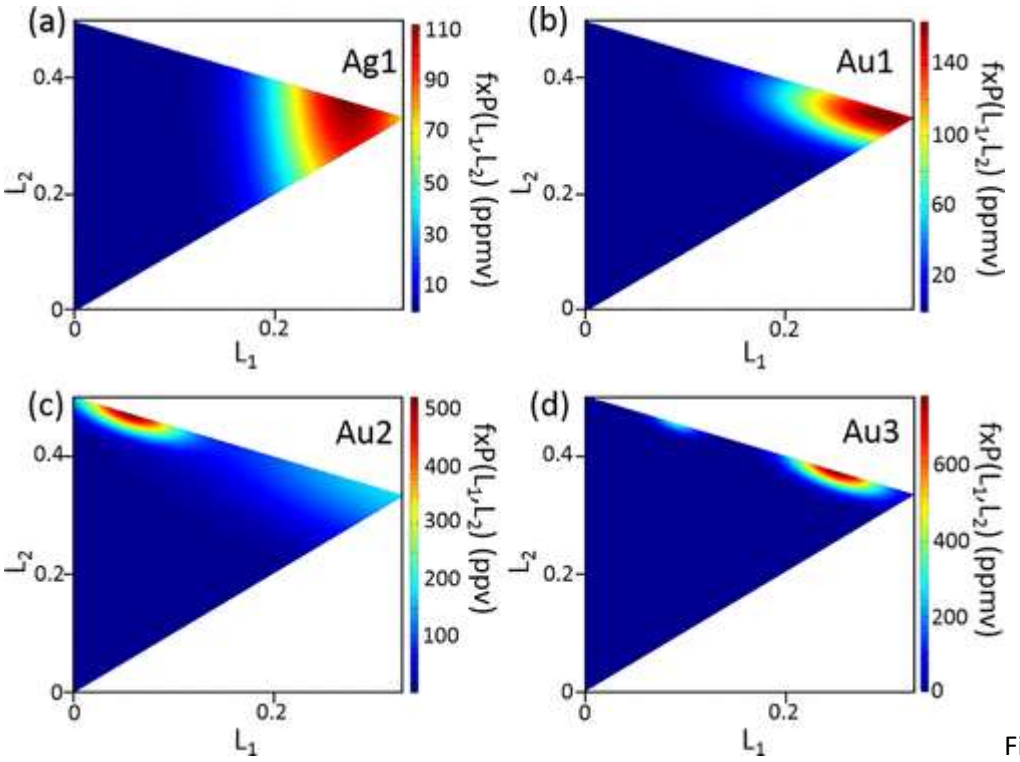

Figure 7

Figure 7. Distribution of depolarization parameters of (a) Ag1, (b) Au1, (c) Au2 and (d) Au3 determined by ellipsometry. The Ag1, Au1, Au2, and Au3 NPs volume fraction are estimated at 9.1 ± 0.5, 7.3 ± 0.4, 20.0 ± 1, and 10.0 ± 0.5 ppmv, respectively.

To make a more quantitative comparison between the distribution obtained by TEM and ellipsometry, the distributions of the depolarization parameters along the prolate axis (L2 = L3 = 0.5(1 – L1)) are transformed into distributions of aspect ratio by using eq 9. Note that this equation is established for ellipsoidal NPs. Therefore, according to Constantin, (48) the aspect ratio of nanorods (RNR) is calculated from the aspect ratio of prolate NPs (Rp) by applying the following correction:

$$R_{NR} = \left(1 + \frac{4\gamma}{3}\,\frac{\gamma^2 + 2\gamma + 3/4}{\gamma + 8/15}\right)^{-1/2} \quad (22)$$

where . The comparisons between the aspect ratio distributions of Au2 and Au3 NPs estimated from TEM and ellipsometry are reported in Figure 8. The aspect ratio distributions obtained by ellipsometry are similar to those deduced from TEM images. The position and width of the two components of the bimodal distributions are in good agreement with those determined by TEM. However, it is not the case for their amplitude ratios. This discrepancy can be explained by the fact that the distributions obtained from TEM are number weighted distributions while those obtained from ellipsometry are volume weighted distributions. By considering the ellipsometric beam diameter, the thickness of spacers, the NP volume fraction, and their average volume, we can conclude that the light beam probes approximately 1011 NPs. This suggests that the number of probed NPs by ellipsometry is sufficiently significant to accurately estimate the distribution of the NP aspect ratio.

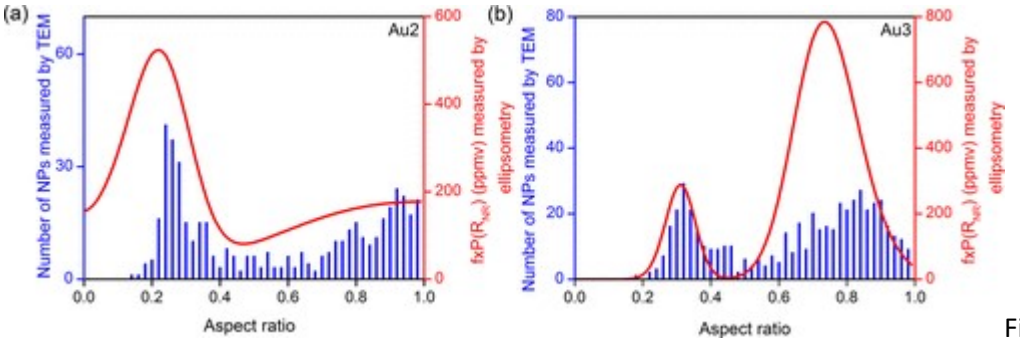

Figure 8

Figure 8. Comparison between the aspect ratio distributions of (a) Au2 and (b) Au3 determined by ellipsometry (solid line) and TEM (bar).

As shown in Figure 9, ellipsometric measurements enables the determination of the real part and imaginary part of the effective refractive index of the colloids. Note that the real part of the effective refractive index of Au1, Au2 and Au3 is close to the refractive index of water (Figure 9a). Indeed, according to the Wiener bounds (49) and in the limit of small volume fraction of NPs, the real part of the effective refractive index of the solution must tend toward the real part of the refractive index of the matrix (the water here). Unlike, absorption spectroscopy, ellipsometry is sensitive to the refractive index of the solvent. The real part of the refractive index of Ag1 is slightly larger than that of water. Indeed, this solution contains 1 wt % AGP which has a refractive index larger than the water one. (50, 51) In other words, the real part of the effective refractive index of Ag1 reveals the presence of AGP in water. The plasmon bands of NPs are clearly observed on the effective extinction spectra (Figure 9b–d). The same holds for the interband transition thresholds, located at 2.5 and 3.9 eV for Au and Ag, respectively. It is also worth noting that, as expected, the extinction coefficient of Au colloids increases with the volume fraction of NPs. Note that the extinction coefficient of colloids is in the range that can be measured by the ellipsometric cell (Figure 3c,d). Au1 and Ag1 extinction spectra are dominated by a band located at 2.35 and 2.9 eV, respectively, assigned to the plasmon band of nearly spherical NPs. On the Ag1 spectra, the shoulder observed at 3.4 eV is an artifact which comes from the Palik dielectric function of silver. Indeed, the tabulated dielectric function of Ag is made by juxtaposing, at 3.4 eV, the Winsemius et al. (52) and the Leveque et al. (53) databases. The plasmon band located at 2.35 eV is also observed on the Au2 and Au3 spectra. In addition, Au2 and Au3 spectra have a band located at 1.7 and 1.5 eV, respectively, which corresponds to the longitudinal plasmon band of gold nanorods. The slight red shift observed for Au3 is attributed to the shorter aspect ratio of Au nanorods.

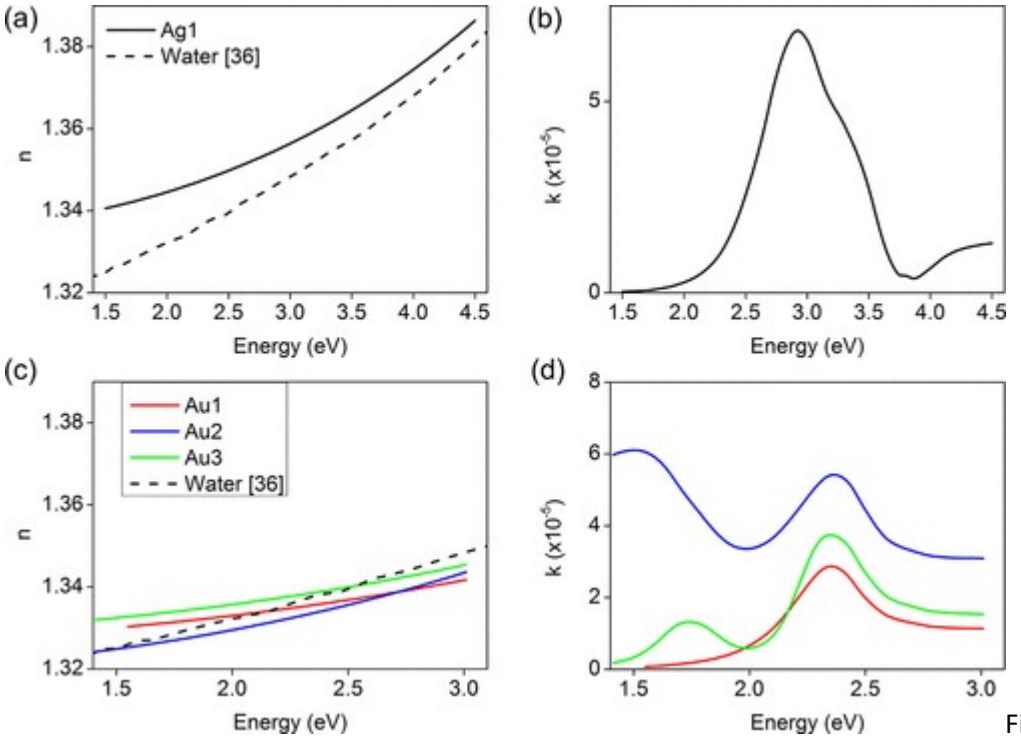

Figure 9

Figure 9. (a,c) Real part and (b,d) imaginary part of the effective dielectric function of (a,b) Ag1 and (c,d) Au1, Au2, and Au3. The Ag1, Au1, Au2, and Au3 NPs volume fraction are 9.1 ± 0.5, 7.3 ± 0.4, 20.0 ± 1, and 10.0 ± 0.5 ppmv, respectively. The real part of refractive index of water given by Palik (36) is also reported.

Conclusion

In summary, we have developed a cell to perform ellipsometric measurements on liquids. This cell, which consists of a silicon substrate, a spacer, and an isosceles prism, was used to characterize Ag and Au colloids. Simulations have revealed that the ellipsometric cell pushes the detection limit of ellipsometry to NPs toward the ppmv range. Contrary to transmission spectroscopy, ellipsometry is sensitive to both the real part and the imaginary part of the refractive index and the measurements can be performed on a small volume of solution. Thus, the complex effective refractive index of colloids as well as the volume fraction and the shape distribution of NPs have been determined from the ellipsometric measurements by analyzing them with an effective medium theory which takes into account the NP shape distribution. These distributions are close to the ones obtained from TEM. Contrary to TEM measurements, the NP shape distribution is obtained from a large number of NPs estimated at 1011 NPs. This demonstrates that ellipsometry coupled to the liquid cell provides a robust and straightforward tool for the characterization of the NP shape, concentration and optical properties. This ellipsometric cell can be used to measure the optical properties of a large number of solutions. The unique constrain concerns the trade-off between the spacer thickness and the magnitude of the extinction coefficient. By adapting the modeling to the investigated nanostructures, we predict the characterization of other nanomaterials with this ellipsometric cell, such as colloidal solutions composed of smaller or larger metallic NPs, NP assembly, semiconducting NPs, or carbon

nanotubes. The characterization of these nanomaterials is beyond the scope of this paper and will be considered in a future paper.

1McFarland, A. D.; Van Duyne, R. P. Single silver nanoparticles as real-time optical sensors with zeptomole sensitivity Nano Lett. 2003, 3, 1057– 1062 DOI: 10.1021/nl034372s [ACS Full Text ACS Full Text], [CAS], Google Scholar

2Wang, F.; Liu, X.; Lu, C.-H.; Willner, I. Cysteine-mediated aggregation of Au nanoparticles: the development of a H2O2 sensor and oxidase based biosensors ACS Nano 2013, 7, 7278– 7286 DOI: 10.1021/nn402810x [ACS Full Text ACS Full Text], Google Scholar

3Xianyu, Y.; Wang, Z.; Jiang, W. A plasmonic nanosensor for immunoassay via enzyme-triggered click chemistry ACS Nano 2014, 8, 12741– 12747 DOI: 10.1021/nn505857g [ACS Full Text ACS Full Text], [CAS], Google Scholar

4Schofield, C. L.; Haines, A. H.; Field, R. A.; Russell, D. A. Silver and Gold Glyconanoparticles for Colorimetric Bioassays Langmuir 2006, 22, 6707– 6711 DOI: 10.1021/la060288r [ACS Full Text ACS Full Text], [CAS], Google Scholar

5Zhang, Y.; Liu, Q.; Mundoor, H.; Yuan, Y.; Smalyukh, I. Metal nanoparticle dispersion, alignment and assembly in nematic liquid crystals for applications in switchable plasmonic color filters and E-polarizers ACS Nano 2015, 9, 3097– 3108 DOI: 10.1021/nn5074644 [ACS Full Text ACS Full Text], Google Scholar

6Zhang, X.-Y.; Hu, A.; Zhang, T.; Lei, W.; Xue, X.-J.; Zhou, Y.; Duley, W. W. Self-assembly of large-scale and ultrathin silver nanoplate films with tunable plasmon resonance properties ACS Nano 2011, 5, 9082– 9092 DOI: 10.1021/nn203336m [ACS Full Text ACS Full Text], [CAS], Google Scholar

7Kreibig, U.; Vollmer, M. Optical properties of metal clusters; Springer: Berlin, Germany, 1995.[Crossref], Google Scholar

8Kelly, L.; Coronado, E.; Zhao, L. L.; Schatz, G. C. The optical properties of metal nanoparticles: the influence of size, shape, and dielectric environment J. Phys. Chem. B 2003, 107, 668– 677 DOI: 10.1021/jp026731y [ACS Full Text ACS Full Text], [CAS], Google Scholar

9Noguez, C. Surface plasmons on metal nanoparticles: the influence of shape and physical environement J. Phys. Chem. C 2007, 111, 3806– 3819 DOI: 10.1021/jp066539m [ACS Full Text ACS Full Text], Google Scholar

10Bois, L.; Chassagneux, F.; Desroches, C.; Battie, Y.; Destouches, N.; Gilon, N.; Parola, S.; Stéphan, O. Electroless growth of silver nanoparticles into mesostructured silica block copolymer films Langmuir 2010, 26, 8729– 8736 DOI: 10.1021/la904491v [ACS Full Text ACS Full Text], Google Scholar

11Peña, O.; Rodriguez-Fernandez, L.; Rodriguez-Iglesias, V.; Kellermann, G.; Crespo-Sosa, A.; Cheang-Wong, J. C.; Silva-Pereyra, H. G.; Arenas-Alatorre, J.; Oliver, A. Determination of the size distribution of metallic nanoparticles by optical extinction spectroscopy Appl. Opt. 2009, 48, 566– 572 DOI: 10.1364/AO.48.000566 [Crossref], [PubMed], [CAS], Google Scholar

12Rodriguez-Iglesias, V.; Peña-Rodriguez, O.; Silva-Pereyra, H. G.; Rodriguez-Fernandez, L.; Kellermann, G.; Cheang-Wong, J. C.; Crespo-Sosa, A.; Oliver, A. Elongated gold nanoparticles obtained

by ion implantation in silica: characterization and T-matrix simulations J. Phys. Chem. C 2010, 114, 746–751 DOI: 10.1021/jp906845u [ACS Full Text ACS Full Text], Google Scholar

13Henry, C. R. Morphology of supported nanoparticles Prog. Surf. Sci. 2005, 80, 92– 116 DOI: 10.1016/j.progsurf.2005.09.004 [Crossref], [CAS], Google Scholar

14Eustis, S.; El-Sayed, M. A. Determination of the aspect ratio statistical distribution of gold nanorods in solution from a theoretical fit of the observed inhomogeneously broadened longitudinal plasmon resonance absorption spectrum J. Appl. Phys. 2006, 100, 044324 DOI: 10.1063/1.2244520 [Crossref], [CAS], Google Scholar

15Slyusarenko, K.; Abécassis, B.; Davidson, P.; Constantin, D. Morphology of gold nanoparticles determined by full-curve fitting of the light absorption spectrum. Comparison with X-ray scattering and electron microscopy data Nanoscale 2014, 6, 13527– 13534 DOI: 10.1039/C4NR04155K [Crossref], Google Scholar

16Resano-Garcia, A.; Battie, Y.; En Naciri, A.; Akil, S.; Chaoui, N. Experimental and theoretical determination of the plasmonic responses and shape distribution of colloidal metallic nanoparticles J. Chem. Phys. 2015, 142, 134108 DOI: 10.1063/1.4916917 [Crossref], [PubMed], [CAS], Google Scholar

17Battie, Y.; Resano-Garcia, A.; En Naciri, A.; Akil, S.; Chaoui, N. Determination of morphological characteristics of metallic nanoparticles based on modified Maxwell-Garnett fitting of optical responses Appl. Phys. Lett. 2015, 107, 143104 DOI: 10.1063/1.4932638 [Crossref], Google Scholar

18Resano-Garcia, A.; Battie, Y.; En Naciri, A.; Chaoui, N. Interaction of a converging laser beam with a Ag colloidal solution during the ablation of a Ag target in water Nanotechnology 2016, 27, 215705 DOI: 10.1088/0957-4484/27/21/215705 [Crossref], Google Scholar

19Battie, Y.; Izquierdo-Lorenzo, I.; Resano-Garcia, A.; En Naciri, A.; Akil, S.; Adam, P. M.; Jradi, S. Determination of gold nanoparticle shape from absorption spectroscopy and ellipsometry Appl. Surf. Sci. 2016, DOI: 10.1016/j.apsusc.2016.12.167 [Crossref], Google Scholar

20Oates, T. W. H. Real time spectroscopic ellipsometry of nanoparticle growth Appl. Phys. Lett. 2006, 88, 213115 DOI: 10.1063/1.2206870 [Crossref], Google Scholar

21Oates, T. W. H.; Christalle, E. Real-time spectroscopic ellipsometry of silver nanoparticle formation in poly (vinyl alcohol) thin films J. Phys. Chem. C 2007, 111, 182– 187 DOI: 10.1021/jp065081l [ACS Full Text ACS Full Text], Google Scholar

22Battie, Y.; Izquierdo-Lorenzo, I.; Resano-Garcia, A.; En Naciri, A.; Akil, S.; Adam, P. M.; Jradi, S. How to determine the morphology of plasmonic nanocrystals without transmission electron microscopy? J. Nanopart. Res. 2016, 18, 217 DOI: 10.1007/s11051-016-3533-8 [Crossref], Google Scholar

23Pecharroman, C.; Della Gaspera, E.; Martucci, A.; Escobar-Galindod, R.; Mulvaney, P. Determination of the optical constants of gold nanoparticles from thin-film spectra J. Phys. Chem. C 2015, 119, 9450–9459 DOI: 10.1021/jp512611m [ACS Full Text ACS Full Text], [CAS], Google Scholar

24Battie, Y.; Destouches, N.; Chassagneux, F.; Jamon, D.; Bois, L.; Moncoffre, N.; Toulhoat, N. Optical properties of silver nanoparticles thermally grown in a mesostructured hybrid silica film Opt. Mater. Express 2011, 1, 1019– 1033 DOI: 10.1364/OME.1.001019 [Crossref], [CAS], Google Scholar

25Toudert, J.; Simonot, L.; Camelio, S.; Babonneau, D. Advanced optical effective medium modeling for a single layer of polydisperse ellipsoidal nanoparticles embedded in a homogeneous dielectric

medium: Surface plasmon resonances Phys. Rev. B: Condens. Matter Mater. Phys. 2012, 86, 045415 DOI: 10.1103/PhysRevB.86.045415 [Crossref], [CAS], Google Scholar

26Battie, Y.; En Naciri, A.; Chamorro, W.; Horwat, D. Generalized effective medium theory to extract the optical properties of two-dimensional nonspherical metallic nanoparticle layers J. Phys. Chem. C 2014, 118, 4899 DOI: 10.1021/jp4119343 [ACS Full Text ACS Full Text], [CAS], Google Scholar

27Oates, T. W. H.; Mücklich, A. Evolution of plasmon resonances during plasma deposition of silver nanoparticles Nanotechnology 2005, 16, 2606 DOI: 10.1088/0957-4484/16/11/023 [Crossref], [CAS], Google Scholar

28Wormeester, H.; Kooij, E. S.; Mewe, A.; Rekveld, S.; Poelsema, B. Ellipsometric characterisation of heterogeneous 2D layers Thin Solid Films 2004, 455–456, 323– 334 DOI: 10.1016/j.tsf.2004.01.019 [Crossref], Google Scholar

29Kubo, S.; Diaz, A.; Tang, Y.; Mayer, T. S.; Khoo, I. C.; Mallouk, T. E. Tunability of the refractive index of gold nanoparticle dispersions Nano Lett. 2007, 7, 3418– 3423 DOI: 10.1021/nl071893x [ACS Full Text ACS Full Text], [CAS], Google Scholar

30Wang, L.; Zhao, C.; Duits, M. H. G.; Mugele, F.; Siretanu, I. Detection of ion adsorption at solid-liquid interfaces using internal reflection ellipsometry Sens. Actuators, B 2015, 210, 649– 655 DOI: 10.1016/j.snb.2014.12.127 [Crossref], [CAS], Google Scholar

31Benjamins, J. W.; Jönsson, B.; Thuresson, K.; Nylander, T. New experimental setup to use ellipsometry to study liquid–liquid and liquid–solid Interfaces Langmuir 2002, 18, 6437– 6444 DOI: 10.1021/la025588x [ACS Full Text ACS Full Text], Google Scholar

32Benjamins, J. W.; Thuresson, K.; Nylander, T. Ellipsometry Studies of Nonionic Surfactant Adsorption at the Oil–Water Interface Langmuir 2005, 21, 149– 159 DOI: 10.1021/la049848h [ACS Full Text ACS Full Text], Google Scholar

33Blomqvist, B. R.; Benjamins, J. W.; Nylander, T.; Arnebrant, T. Ellipsometric characterization of ethylene oxide-butylene oxide diblock copolymer adsorption at the air-water interface Langmuir 2005, 21, 5061– 5068 DOI: 10.1021/la0468040 [ACS Full Text ACS Full Text], Google Scholar

34Broch, L.; Johann, L.; Stein, N.; Zimmer, A.; Beck, R. Real time in situ ellipsometric and gravitometric monitoring for electrochemistry experiments Rev. Sci. Instrum. 2007, 78, 064101 DOI: 10.1063/1.2743273 [Crossref], [PubMed], [CAS], Google Scholar

35Nador, J.; Kalas, B.; Saftics, A.; Agocs, E.; Kozma, P.; Korosi, L.; Szekacs, I.; Fried, M.; Horvath, R.; Petrik, P. Plasmon-enhenced two-channel in situ Kretschmann ellipsometry of protein adsorption, cellular adhesion and polyelectrolyte deposition on titania nanostructure Opt. Express 2016, 24, 4812–4823 DOI: 10.1364/OE.24.004812 [Crossref], Google Scholar

36Palik, E. D. Handbook of Optical Constants of Solids; Academic Press: New York, 1985.Google Scholar

37Bohren, C. F.; Huffman, D. R. Absorption and scattering by a sphere. In Absorption and Scattering of Light by Small Particles; Wiley: Germany, 1998.[Crossref], Google Scholar

38Fujiwara, H. Spectroscopic ellipsometry: Principles and applications; Wiley, 2007.[Crossref], Google Scholar

39Forcht, K.; Gombert, A.; Joerger, R.; Kohl, M. Incoherent superposition in ellipsometric measurements Thin Solid Films 1997, 302, 43– 50 DOI: 10.1016/S0040-6090(96)09555-7 [Crossref], Google Scholar

40Kildemo, M.; Ossikovski, T.; Stchakovsky, M. measurement of the absorption edge of thick transparent substrates using the incoherent reflection model and spectroscopic UV-visible-near IR ellipsometry Thin Solid Films 1998, 313–314, 108– 113 DOI: 10.1016/S0040-6090(97)00779-7 [Crossref], Google Scholar

41Stchakovsky, M.; Battie, Y.; En Naciri, A. An original method to determine complex refractive index of liquids by spectroscopic ellipsometry and illustrated applications Appl. Surf. Sci. 2016, DOI: 10.1016/j.apsusc.2016.12.001 [Crossref], Google Scholar

42Trügler, A.; Tinguely, J. C.; Krenn, J. R.; Hohenau, A.; Hohenester, U. Influence of surface roughness on the optical properties of plasmonic nanoparticles Phys. Rev. B: Condens. Matter Mater. Phys. 2011, 83, 081412 DOI: 10.1103/PhysRevB.83.081412 [Crossref], [CAS], Google Scholar

43Hlawacek, G.; Ahmad, I.; Smithers, M. A.; Kooij, E. S. To see or not to see: Imaging surfactant coated nano-particles using HIM and SEM Ultramicroscopy 2013, 135, 89– 94 DOI: 10.1016/j.ultramic.2013.07.010 [Crossref], [PubMed], [CAS], Google Scholar

44Kékicheff, P.; Spalla, O. Refractive index of thin aqueous films confined between two hydrophobic surfaces Langmuir 1994, 10, 1584– 1591 DOI: 10.1021/la00017a043 [ACS Full Text ACS Full Text], [CAS], Google Scholar

45Johnson, P. B.; Christy, R. W. Optical constants of noble metals Phys. Rev. B 1972, 6, 4370 DOI: 10.1103/PhysRevB.6.4370 [Crossref], [CAS], Google Scholar

46Jiang, Y.; Pillai, S.; Green, M. A. Realistic Silver Optical Constants for Plasmonics Sci. Rep. 2016, 6, 30605 DOI: 10.1038/srep30605 [Crossref], [PubMed], [CAS], Google Scholar

47Levenberg, K. A. Method for the solution of certain problems in least squares Q. Appl. Math. 1944, 2, 164– 168 DOI: 10.1090/qam/10666 [Crossref], Google Scholar

48Constantin, D. Why the aspect ratio? Shape equivalence for the extinction spectra of gold nanoparticles Eur. Phys. J. E: Soft Matter Biol. Phys. 2015, 38 (11) 1– 6 DOI: 10.1140/epje/i2015-15116-2 [Crossref], [PubMed], [CAS], Google Scholar

49Aspnes, D. E. Bounds on allowed values of the effective dielectric function of two-component composites at finite frequencies Phys. Rev. B: Condens. Matter Mater. Phys. 1982, 25, 1358 DOI: 10.1103/PhysRevB.25.1358 [Crossref], Google Scholar

50Phillips, G. O.; Williams, P. A. In Food hydrocolloids; Nishinari, K.; Doi, E., Eds.; Springer, 1994.Google Scholar

51Akil-Jradi, S.; Jradi, S.; Plain, J.; Bijeon, J. L.; Sanchez, C.; Bachelot, R.; Royer, P. Chem. Commun. 2011, 47, 2444– 2446 DOI: 10.1039/C0CC05212D [Crossref], Google Scholar

52Winsemius, P.; Van Kampen, F. F.; Lengkeek, H. P.; Van Went, C. G. J. Phys. F: Met. Phys. 1976, 6, 1583 DOI: 10.1088/0305-4608/6/8/017 [Crossref], [CAS], Google Scholar

53Leveque, G.; Olson, C. G.; Lynch, D. W. Phys. Rev. B: Condens. Matter Mater. Phys. 1983, 27, 4654 DOI: 10.1103/PhysRevB.27.4654 [Crossref], Google Scholar